Earth Planet. Sci. Lett. 687 (2026) 120089

Contents lists available at ScienceDirect

Earth and Planetary Science Letters

journal homepage: www.elsevier.com/locate/epsl

Effect of realistic heat flux patterns on geodynamo simulations

T. Frasson [a,b,*], N. Schaeffer [b], H.-C. Nataf [b], S. Labrosse [c]

[a] School of Earth and Environment, University of Leeds, Leeds, LS29JT, UK
[b] Univ. Grenoble Alpes, Univ. Savoie Mont Blanc, CNRS, IRD, Univ. Gustave Eiffel, ISTerre, Grenoble, 38000, France
[c] ENS de Lyon, Universite Lyon-1, LGL-TPE, 46 allee d'Italie, Lyon, 69007, France

ARTICLE INFO

Editor: Dr H Thybo

Keywords:
Magnetic reversals
Numerical simulations
Core-mantle boundary heat flux
Zonal flows

ABSTRACT

The heat flux pattern at the core-mantle boundary (CMB) is known to affect the stability of the magnetic dipole in numerical simulations of the geodynamo. Variations in this pattern could explain the changes in the frequency of magnetic reversals through geological times. However, the exact relation between heat flux heterogeneities and the dynamo behaviour is still unclear. In this study, we explore the effect on numerical dynamo simulations of two heat flux patterns extracted from mantle models: one is representative of the present-day, and a second is dominated by a differential cooling between the equator and higher latitudes. Such a cooling contrast between the equatorial and polar regions, in isolation, has been shown to be key in controlling the propensity for dipole reversals. We apply these patterns on three dynamo simulations with varying magnetic field strength and zonal flow amplitudes, representing different potential dynamical states of the core. We find that the destabilization of the dipole occurs when the heat flux pattern disrupts the westward flows in the core, confirming earlier results obtained using idealized heat flux geometries. We also find the same link between the occurrence of reversals and the ratio of zonal antisymmetric magnetic to kinetic energy. More surprisingly, the dipole is destabilized when the heat flux pattern exerts even a slightly stronger cooling near the equator than in the polar regions, demonstrating the crucial role of latitudinal variations in the CMB heat flux.

1. Introduction

Earth's magnetic field is produced by dynamo action in Earth's core through a process called the geodynamo. This geodynamo is believed to be mainly powered by the release of light elements and latent heat at the bottom of the outer core as a result of inner core crystallization (Lister and Buffett, 1995; Labrosse, 2015). Despite having a smaller contribution to the convective power in the core, the heat flux at the top of the core can affect the behaviour of the geodynamo. This heat flux at the core-mantle boundary (CMB) is probably heterogeneous, with a peak-to-peak heterogeneity amplitude that could easily be larger than the mean heat flux (Nakagawa and Tackley, 2008; Dannberg et al., 2024; Frasson et al., 2024). Seismic tomography can constrain lateral variations in seismic characteristics in the lower mantle (Masters et al., 1996; Cottaar and Lekic, 2016; Durand et al., 2017). The CMB heat flux can be deduced from tomographic images assuming proportionality between velocity anomalies and temperature (hereafter termed "tomographic pattern") (Glatzmaier et al., 1999; Kutzner and Christensen, 2004; Olson et al., 2010; Mound and Davies, 2023; Terra-Nova and Amit, 2024), or considering more complex relations that account for compositional effects (Amit and Choblet, 2009; Amit et al., 2015b; Choblet et al., 2023). Heat flux heterogeneities based on the tomographic pattern have been shown to affect core dynamics in multiple ways. This pattern can, for example, create local stratifications that could explain seismic observations without requiring a global stratification at the top of the core (Mound et al., 2019). Longitudinal heterogeneities in the CMB heat flux could also be responsible for the observed clustering of virtual geomagnetic poles (Kutzner and Christensen, 2004) and for long-lived features of the magnetic field (Mound and Davies, 2023).

On long time scales, the most striking feature of the geodynamo is the variation in the reversal frequency of the magnetic dipole (Cox et al., 1964; Lowrie and Kent, 2004). In numerical geodynamo simulations, an equatorial cooling of the core and equatorially antisymmetric heat flux patterns have been shown to favour weak reversing dipoles (Olson et al., 2010; Frasson et al., 2025). The present-day heat flux pattern is usually found to destabilize the dipole (Olson et al., 2010; Olson and Amit, 2014), although recent studies suggest that this pattern could stabilize it when larger heterogeneity amplitudes are used (Mound and Davies, 2023; Terra-Nova and Amit, 2024). The CMB heat flux in the geological past is difficult to retrieve. Olson et al. (2013) couple geodynamo simulations with outputs of a mantle convection model to predict the variations in the control parameters and thermal boundary conditions

* Corresponding author.
E-mail address: t.a.frasson@leeds.ac.uk (T. Frasson).

https://doi.org/10.1016/j.epsl.2026.120089
Received 24 July 2025; Received in revised form 17 February 2026; Accepted 2 May 2026
Available online 8 May 2026

of the simulations. They show that varying heat flux heterogeneities at the CMB helps explaining the observed variations in the reversal frequency.

However, this approach suffers from two main limitations. First, predictions from mantle convection models vary depending on the model assumptions (Zhang and Zhong, 2011; Dannberg et al., 2024). These predictions are furthermore limited by our poor knowledge of plate tectonics prior to the Pangea assembly (Merdith et al., 2017; Seton et al., 2023), and by the additional complexity of true polar wander that can render the reference frame of mantle convection models different from the core reference frame (Frasson et al., 2024). Maybe because of these uncertainties, CMB heat flux variations predicted by plate-driven mantle convection models show only weak and non-robust correlations with the reversal frequency (Zhang and Zhong, 2011; Biggin et al., 2012; Choblet et al., 2016). A second source of limitations lies in the fact that most numerical models of the geodynamo do not reproduce the regime expected for the Earth's core in which the Lorentz force plays a significant dynamical role, while the influence of viscosity is negligible (Soderlund et al., 2012; Dormy, 2016; Nataf and Schaeffer, 2024). Although conditions approaching the asymptotic regime of the Earth's core have been reached in numerical simulations (Aubert et al., 2017; Schaeffer et al., 2017; Aubert, 2023; Lin et al., 2025), only very short time scales can be simulated. The use of more moderate parameter regimes is required in order to study the long-term behaviour of the geodynamo, such as reversals. In a previous study, we showed that the effect on geodynamo simulations of heat flux heterogeneities largely depends on the strength of westward flows within the core, reversals being favoured by the disruption of these zonal flows (Frasson et al., 2025).

We choose to follow an exploratory approach by selecting two heat flux patterns representative of specific mantle configurations extracted from mantle convection models rotated in the reference frame of the core by Frasson et al. (2024). The present-day heat flux pattern in a plate-driven mantle convection model (case MF0 in Frasson et al. (2024)) is considered representative of the present-day configuration. We also use a time-averaged heat flux pattern of a self-consistent mantle convection model in which hot primordial material stays preferentially at the poles (case MC1 in Frasson et al. (2024)). We exploit three geodynamo simulations already used in Frasson et al. (2025) with variable strength of westward flows. Polar versus equatorial cooling (i.e. the sign of the degree 2 order 0 spherical harmonic component) has the largest impact on the dipole stability (Frasson et al., 2025). Thus, we interpret our results focusing particularly on the sign and amplitude of this component, and we also use the opposite patterns (i.e. using negative amplitudes) to understand how it affects the dynamo behaviour.

2. Methods

2.1. Geodynamo models and diagnostics

We model Earth's core by a spherical shell of outer radius r_o and inner radius r_i with an aspect ratio $r_i/r_o = 0.35$ and a shell thickness $D = r_o - r_i$. This spherical shell rotates at a rate Ω around the z axis. The acceleration of gravity varies with radius as $\mathbf{g} = g_o \frac{r}{r_o}\hat{\mathbf{r}}$ where g_o is the acceleration of gravity at the top of the core, and $\hat{\mathbf{r}}$ is the unit vector in the radial direction. The liquid iron is modelled with a viscosity ν and a magnetic diffusivity η. In Earth's core, convection originates from temperature (T) and composition (χ) gradients that both contribute to density gradients. For simplicity, we use a codensity approach (Braginsky and Roberts, 1995) that combines temperature and composition into a single variable. Calling ρ_0 the reference density of the fluid, α the thermal expansion coefficient, and β the compositional expansion coefficient, the codensity is defined as $C = \rho_0(\alpha T + \beta\chi)$. The codensity diffusivity is called κ. We use the Boussinesq approximation to solve for the velocity $\mathbf{u}$ and the magnetic field $\mathbf{B}$, as well as the codensity. Convection is driven by a fixed positive codensity flux q_i at the bottom of the core. The total codensity flux integrated over the inner core boundary is $F_i = 4\pi r_i^2 q_i$. The mean codensity flux at the top of the core q_o is set to 0, meaning that the top of the core is isentropic on average. Although representing a particular case, an isentropic CMB heat flux is plausible in Earth's core (Labrosse, 2015; Davies, 2015). The heat flux pattern added in addition to this isentropic mean flux has a null spatial average, ensuring that this isentropic condition is preserved on average over the CMB. Both boundaries have no-slip conditions for the flow. The magnetic field matches a potential field at the CMB and the inner core is conducting with the same conductivity as the outer core. We use the XSHELLS code to solve the Navier-Stokes equations coupled to the induction equation (Schaeffer et al., 2017; Guervilly et al., 2019). The equation details are given in Frasson et al. (2025). To fully define the simulations we need to set the values of the four non-dimensional parameters corresponding to the Rayleigh number Ra, the Ekman number E, the Prandtl number Pr, and the magnetic Prandtl number Pm. These numbers are defined as

$$Ra = \frac{g_o F_i D^2}{4\pi\kappa\nu^2\rho_0}, \quad (1)$$

$$E = \frac{\nu}{\Omega D^2}, \quad (2)$$

$$Pr = \frac{\nu}{\kappa}, \quad (3)$$

$$Pm = \frac{\nu}{\eta}. \quad (4)$$

We call the kinetic energy integrated over the fluid outer core E_u and the magnetic energy integrated over the outer core and inner core E_b. The flow RMS velocity U is quantified using the magnetic Reynolds number

$$Rm = \frac{UD}{\eta}. \quad (5)$$

The amplitude of the magnetic field B is quantified using the Elsasser number

$$\Lambda = \frac{B^2}{\rho\Omega\eta\mu_0}. \quad (6)$$

The relative amplitude of the magnetic dipole at the CMB is quantified by the dipolar fraction defined as

$$f_{dip} = \sqrt{\frac{\int_S \mathbf{B_{dip}}^2 \, dS}{\int_S \mathbf{B}^2 \, dS}}, \quad (7)$$

where the integrals are over the CMB, and $\mathbf{B_{dip}}$ is the magnetic dipole at the CMB. We quantify the strength of the zonal flows in the outer core using the mean angular velocity of the fluid relative to the RMS velocity defined as in Frasson et al. (2025) by

$$\Omega_f = \frac{L_z r_o}{I_0 U}, \quad (8)$$

where L_z is the angular momentum of the outer core around the spin axis, and I_0 is the axial moment of inertia of a homogeneous spherical shell. Note that negative values correspond to dominantly westward flows. Frasson et al. (2025) showed that the strength and stability of the magnetic dipole in dynamo simulations with simple heat flux heterogeneities correlate with the zonal and equatorially antisymmetric part of the magnetic to kinetic energy ratio inside the core, quantified by the parameter

$$M^*_{Za} = \frac{\overline{\Lambda_{Za}}}{\overline{Rm_{Za}}^2} \quad (9)$$

where Λ_{Za} is the Elsasser number based on the zonal antisymmetric part of the magnetic field and Rm_{Za} is the magnetic Reynolds number based on the zonal antisymmetric part of the flow. In Eq. (9) and in the following, quantities with overlines correspond to time averages. The transients are removed from all time series by ignoring the first two dipole decay times $t_d = \frac{1}{\pi^2}\frac{r_o^2}{\eta}$, and simulations are integrated for at least two dipole decay times in the converged state.

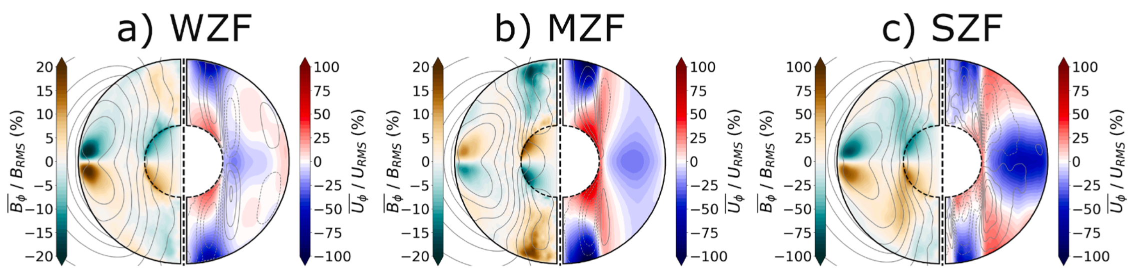

Fig. 1. Meridional cuts showing the azimuthal component of the magnetic field (B_ϕ) and of the velocity (U_ϕ) averaged in time and in the azimuthal direction relative to the root mean square of the fields in the WZF model (a), the MZF model (b) and the SZF model (c). The poloidal field lines are shown as the grey contours. Plain (dashed) field lines indicate clockwise (anticlockwise) flows. In reversing simulations, the magnetic field is multiplied by the sign of the dipole before averaging in time.

Table 1
Input and time-averaged output parameters of the three geodynamo models used in this study. All simulations have $Pr = 1$.

Name	E	Ra ($\times 10^8$)	Pm	$\overline{Rm}$	$\overline{\Lambda}$	$\overline{f_{dip}}$	$\overline{\Omega_f}$ (%)	M^*_{Za} ($\times 10^{-4}$)
WZF	10^{-4}	1.5	3	649	13.1	0.45	−1.2	1.36
MZF	10^{-5}	50	2	987	16.8	0.38	−5.9	0.94
SZF	10^{-5}	5	3	399	16.9	0.61	−17.5	19.92

Because the dynamical state of the core and its evolution across geological time is poorly known, we use three different geodynamo models in this study. These models are characterized by different values of the input non-dimensional parameters. The input and output values of these three models are given in Table 1. The first model has weak zonal flows in the core, we thus call it WZF. A second model has stronger but still moderate zonal flows and is called MZF. The last model, called SZF, has much stronger zonal flows. The WZF, MZF, and SZF models correspond respectively to the E1e-4_hRm, E1e-5_hRm, and E1e-5_SF1 models in Frasson et al. (2025). We show in Fig. 1 meridional slices of the time-averaged magnetic and velocity fields in the models (figures adapted for colour deficient readers are available in supplementary). Outputs from simulations using the WZF, MZF, and SZF models are given in the appendix in Tables A.1–A.3, respectively. Note that hyperdiffusion is used for the WZF model with details in Frasson et al. (2025). All simulations are initiated from the converged state of either the WZF or the MZF simulation without heat flux heterogeneities, with strong and dipolar initial magnetic fields.

2.2. Quantifying complex heat flux heterogeneities

The peak-to-peak amplitude is widely used to quantify heat flux heterogeneities in geodynamo models, both for large-scale patterns (Glatzmaier et al., 1999; Sahoo et al., 2016) and for more complex patterns (Aubert et al., 2013; Amit et al., 2015a; Mound and Davies, 2023; Terra-Nova and Amit, 2024). This definition can be ill-suited when considering complex patterns that have localized extrema. Thus, we quantify the pattern amplitudes with the RMS of the CMB heat flux, called δq_o. This amplitude is computed as

$$\delta q_o = \sqrt{\frac{1}{S}\int_S q_o^2 \, dS}, \tag{10}$$

where S is the CMB surface. We will also define the amplitude of a given spherical harmonic $Y_{l,m}$ of degree l and order m as

$$\left[\delta q_o\right]_{l,m} = \sqrt{\frac{1}{S}\int_S \left[q_o\right]_{l,m}^2 \, dS}, \tag{11}$$

where $\left[q_o\right]_{l,m}$ is the component of q_o projected on $Y_{l,m}$. In the following, we will focus on two amplitudes: the full RMS amplitude δq_o and the RMS amplitude of the degree 2 and order 0 component $\left[\delta q_o\right]_{2,0}$. CMB heat flux heterogeneities are often normalized by the mean heat flux atop the core in geodynamo simulations (Olson et al., 2010; Mound and Davies, 2023; Terra-Nova and Amit, 2024). This definition cannot be used in our case due to the choice of $q_o = 0$. Instead, we scale the heat flux heterogeneities in the geodynamo simulations using the inner boundary flux q_i following (Aubert et al., 2013), such that the normalized pattern amplitude is defined as:

$$\delta q_o^* = \frac{\delta q_o}{q_i}. \tag{12}$$

Following Frasson et al. (2025), the values of δq_o^* for a given pattern are estimated from the dimensional heat flux amplitude δq_o^{th}:

$$\delta q_o^* = \frac{\alpha \delta q_o^{th}}{c_p \dot{r}_i \left(\Delta\rho + \dfrac{\alpha \rho_c L}{c_p}\right)}, \tag{13}$$

where α is the thermal expansivity, $\dot{r}_i$ is the growth rate of the inner core radius, $\Delta\rho$ is the density contrast at the ICB due to changes in the light element concentration, ρ_c is the mean density of the outer core, c_p is the specific heat capacity, and L is the latent heat released due to inner core crystallisation. The dimensional values, from which we estimate the amplitudes of the heat flux patterns used in this study, are listed in Table 2. Note that the values are root mean square amplitudes, and not peak-to-peak amplitudes more commonly used but ill-suited for complex heat flux patterns.

2.3. Heat flux patterns

We selected two heat flux patterns extracted from the mantle convection scenarios described in Frasson et al. (2024). We show the two patterns in Fig. 2(a) and (b) with the red and blue regions corresponding to a larger and weaker heat flux than average, respectively. The amplitudes of degree 1 and degree 2 components relative to the total amplitude are shown in Fig. 2(c) for the two patterns. The sign of the $Y_{2,0}$ component is given at the top of the bars for both cases. This sign is important, as it determines whether the heat flux pattern favours a polar cooling of the core (for a positive $Y_{2,0}$ component) or an equatorial cooling (for a negative $Y_{2,0}$ component). The spatial mean of the patterns has been removed, equivalent to assuming that the spatial mean is equal to the isentropic CMB heat flux. Both patterns have been truncated to a maximum spherical harmonic degree of 50. The t0MF0 pattern (Fig. 2a) is the heat flux pattern at the end of the MF0 and MF* cases in Frasson et al. (2024). This pattern represents the present-day heat flux pattern, under the constraints of a realistic mantle circulation. A large $Y_{2,2}$ component is caused by two antipodal piles of primordial material at the equator. The t0MF0 pattern weakly favours a polar cooling of the core due to a small but positive $Y_{2,0}$ component caused by the high heat flux regions near the poles (red patches in Fig. 2a). This pattern shows a more significant contribution of small scales compared to the usual tomographic pattern that only includes large scales. The t0MF0 pattern is similar to the present-day heat flux pattern in the HF1 model of Zhang

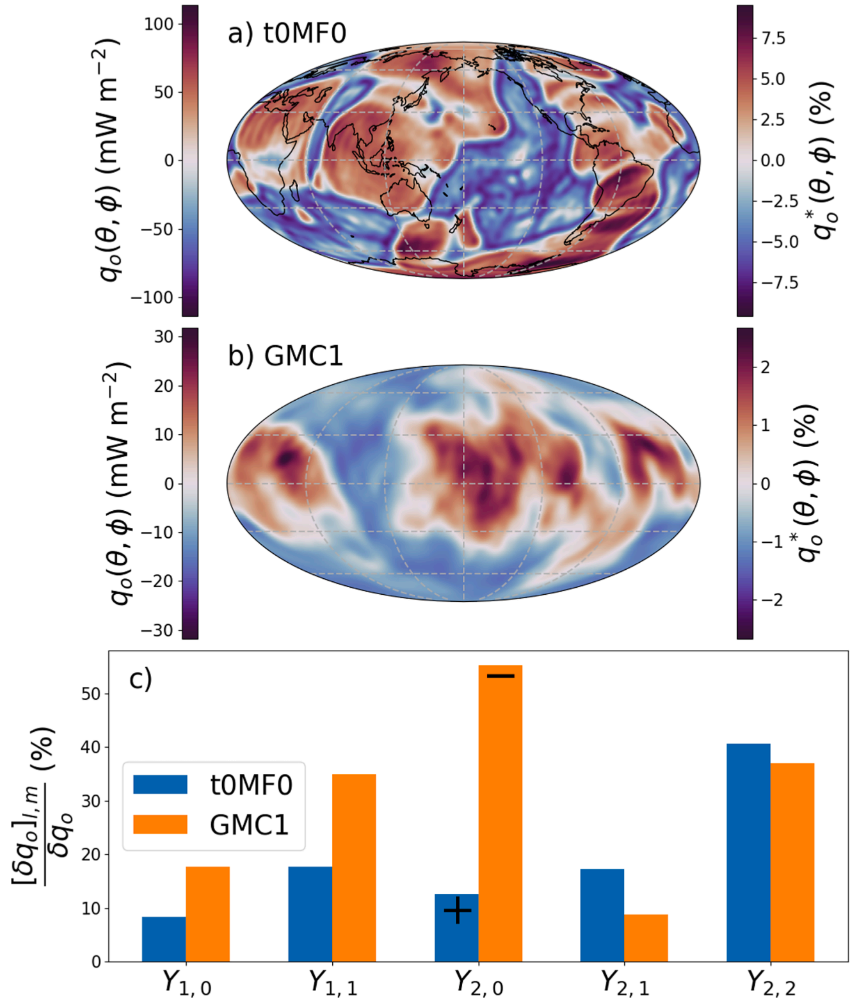

Fig. 2. a) t0MF0 pattern corresponding to the present-day heat flux pattern in the MF0 and MF* cases in Frasson et al. (2024), with the present-day coastlines for reference. b) GMC1 pattern, corresponding to the time-averaged heat flux pattern in the MC1 case in Frasson et al. (2024). Both patterns are shown in a Mollweide projection centered on longitude 180°, and are truncated to a maximum spherical harmonic degree of 50. The colour bar on the left gives the heat flux in mW m^{-2}, the colour bar on the right gives the heat flux normalized by the inner boundary flux ($q_o^* = q_o/q_i$) using the values in Table 2. c) Relative amplitudes of the degree 1 and 2 components in the two patterns.

and Zhong (2011) used by Olson et al. (2013) after truncation to a maximum harmonic degree of 4. Here, we keep the full pattern as presented in Fig. 2(a), truncated at degree 50, leading to small scale heat flux variations.

The second pattern, called GMC1 (Fig. 2b) is the time-averaged heat flux pattern in the MC1 case in Frasson et al. (2024). This case is rotated in the reference frame of the core, and primordial materials stay preferentially near the poles. Thus, this pattern is dominated by a negative $Y_{2,0}$ component with a larger heat flux at the equator than at the poles as evidenced by large red equatorial patches in Fig. 2(b). This pattern is nevertheless more complex than a simple degree 2 order 0 pattern. We note that there are significant low heat flux patches at the equator (appearing in blue in Fig. 2b), imposing large $Y_{1,1}$ and $Y_{2,2}$ components. Because of the time averaging, the smallest scales are removed from this pattern, which is thus intermediate between the large scale pattern studied in Frasson et al. (2025) and direct snapshots taken from mantle convection models. This average pattern represents a realistic depiction of the long-term characteristics of a heat flux pattern dominated by equatorial subductions, damping the less well constrained fluctuating smaller scale structures, and contrasting with the degree 2 order 2 structure of the t0MF0 pattern.

The two patterns crucially differ in the amplitude of the $Y_{2,0}$ component. In order to study the importance of dominant polar versus equatorial cooling, we also considered the opposite patterns (i.e. the t0MF0 and GMC1 patterns with negative amplitudes). In the following, we refer to +t0MF0 and +GMC1 for the patterns shown in Fig. 2, and we will use the notations -t0MF0 and -GMC1 for the negated patterns.

The amplitudes of the two patterns have to be scaled in our simulations. On the right side of the patterns in Fig. 2 we show the scaled amplitude $q_o^* = q_o/q_i$ considering the values in Table 2. Using these values, we obtain an RMS amplitude $\delta q_o^* = 4.30\%$ for t0MF0 and $\delta q_o^* = 0.93\%$ for GMC1. Uncertainties exist on the values given in Table 2, and we thus vary δq_o^* in a range that covers these two values. The GMC1 pattern amplitude is almost 5 times smaller than for the t0MF0 pattern. This is due to the larger space-averaged heat flux in t0MF0 and the time averaging used to obtain GMC1.

3. Results

3.1. Control of heat flux heterogeneities on the reversal behaviour

We show in Fig. 3 the time-averaged dipolar fraction at the CMB in the geodynamo simulations as a function of the amplitude of the t0MF0 and GMC1 pattern. The colour scale in the background gives the amplitude of the $Y_{2,0}$ component alone. The geodynamo behaviours are given by the symbol colours, with the same definition as in Frasson

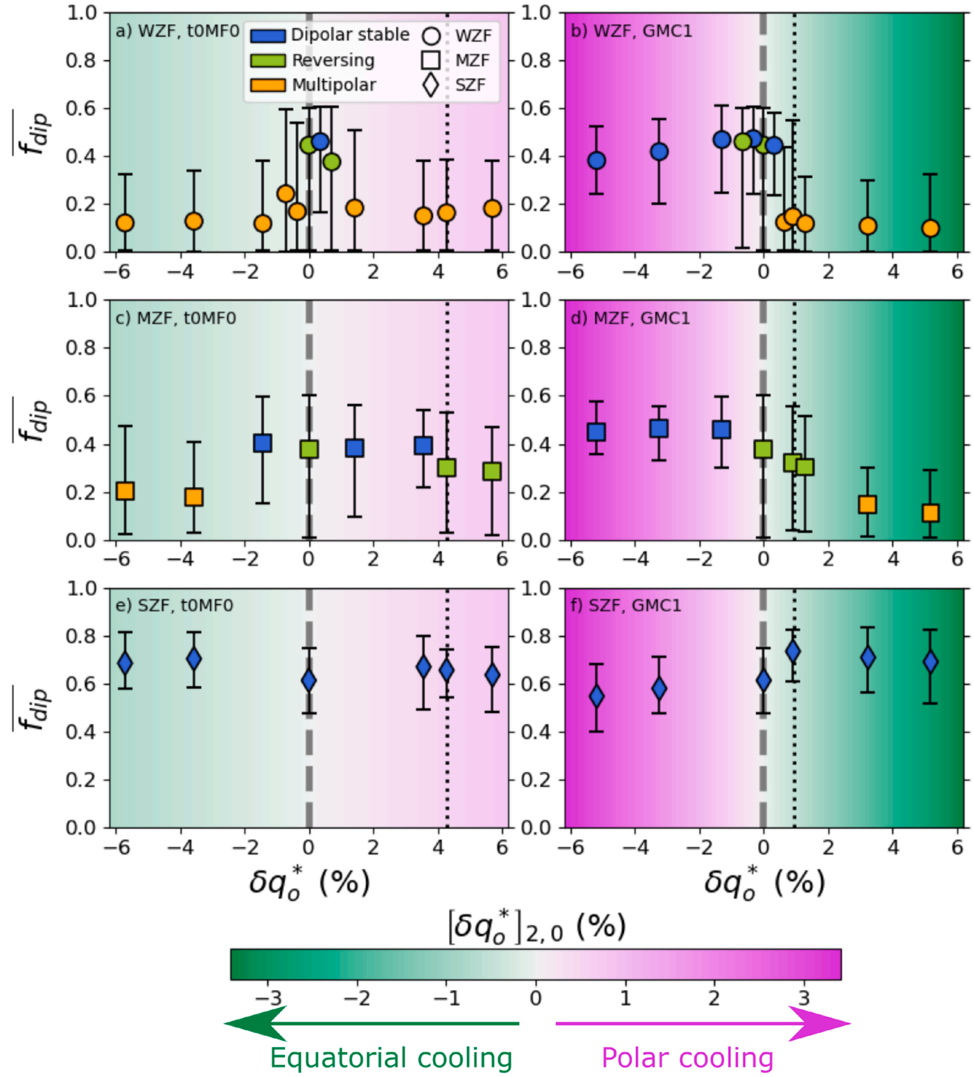

Fig. 3. Time-averaged value of the dipolar fraction as a function of the amplitudes of the heat flux patterns. The corresponding amplitude of the degree 2 order 0 component is shown as the background colour. The marker colours give the behaviour of the dynamo. The geodynamo model is WZF for a and b, MZF for c and d, and SZF for e and f. The heat flux pattern used is t0MF0 for a, c, e, and GMC1 for b, d, f. The heat flux pattern amplitudes estimated from the values in Table 2 are shown by the black dotted lines ($\delta q_o^* = 4.30\,\%$ for t0MF0 and $\delta q_o^* = 0.93\,\%$ for GMC1).

Table 2
Parameters used in the estimation of the pattern amplitudes. The value from Frasson et al. (2024) for δq_o^{th} corresponds to the RMS amplitudes of the CMB heat flux of the t0MF0 and GMC1 patterns respectively.

Symbol	Values	Unit	Reference
ρ_c	1.09×10^4	kg m^{-3}	Olson (2015)
α	1.25×10^{-5}	K^{-1}	Nimmo (2015)
c_p	840	J kg^{-1} K^{-1}	Nimmo (2015)
L	750×10^3	J kg^{-1} K^{-1}	Nimmo (2015)
$\Delta\rho$	560	kg m^{-3}	Nimmo (2015)
$\dot{r}_i$	2.6×10^{-11}	m s^{-1}	Nimmo (2015)
δq_o^{th}	51.2 (t0MF0), 11.1 (GMC1)	mW m^{-2}	Frasson et al. (2024)

et al. (2025): dipolar stable if $\overline{f_{dip}} \geq 0.25$ and the dipole never crosses the equator, reversing if $\overline{f_{dip}} \geq 0.25$ and the dipole crosses the equator at least once, and multipolar if $\overline{f_{dip}} < 0.25$. Note that the "bistable" category in Frasson et al. (2025) is considered as reversing here, for simplicity. The estimated actual amplitude of the two patterns is shown by the dotted lines.

The effect of the +t0MF0 and +GMC1 patterns largely depends on the geodynamo model. The WZF model (Fig. 3a,b) is destabilized by both patterns, as illustrated by the multipolar dynamos obtained even for small pattern amplitudes. This destabilization occurs with the +t0MF0 pattern despite it weakly favouring a polar cooling of the core. The opposite patterns, however, have different effects on the dipole stability. The -t0MF0 pattern destabilizes the dipole even for the smallest amplitude used in this study. The -GMC1 pattern, on the contrary, stabilizes the dipole and prevents reversals, consistent with the strong polar cooling favoured by this pattern.

The MZF model (Fig. 3c) is less affected by the +t0MF0 pattern than the WZF model. This pattern only moderately destabilizes the dipole, without triggering a multipolar dynamo. The -t0MF0 pattern triggers this transition, but at a larger amplitude than for the WZF model. Similarly, the +GMC1 pattern favours a multipolar behaviour with a smoother transition than with the WZF model (Fig. 3d). As for the WZF model, the -GMC1 pattern stabilizes the MZF model.

Finally, the SZF model is weakly affected by heat flux heterogeneities, regardless of the predominance of polar or equatorial cooling (Fig. 3e,f). Opposite to what is observed with the two other models, a dominant equatorial cooling increases the dipolar fraction, a behaviour already noted in Frasson et al. (2025). Interestingly, only the MZF model produces a reversing dynamo when the estimated amplitude of the two

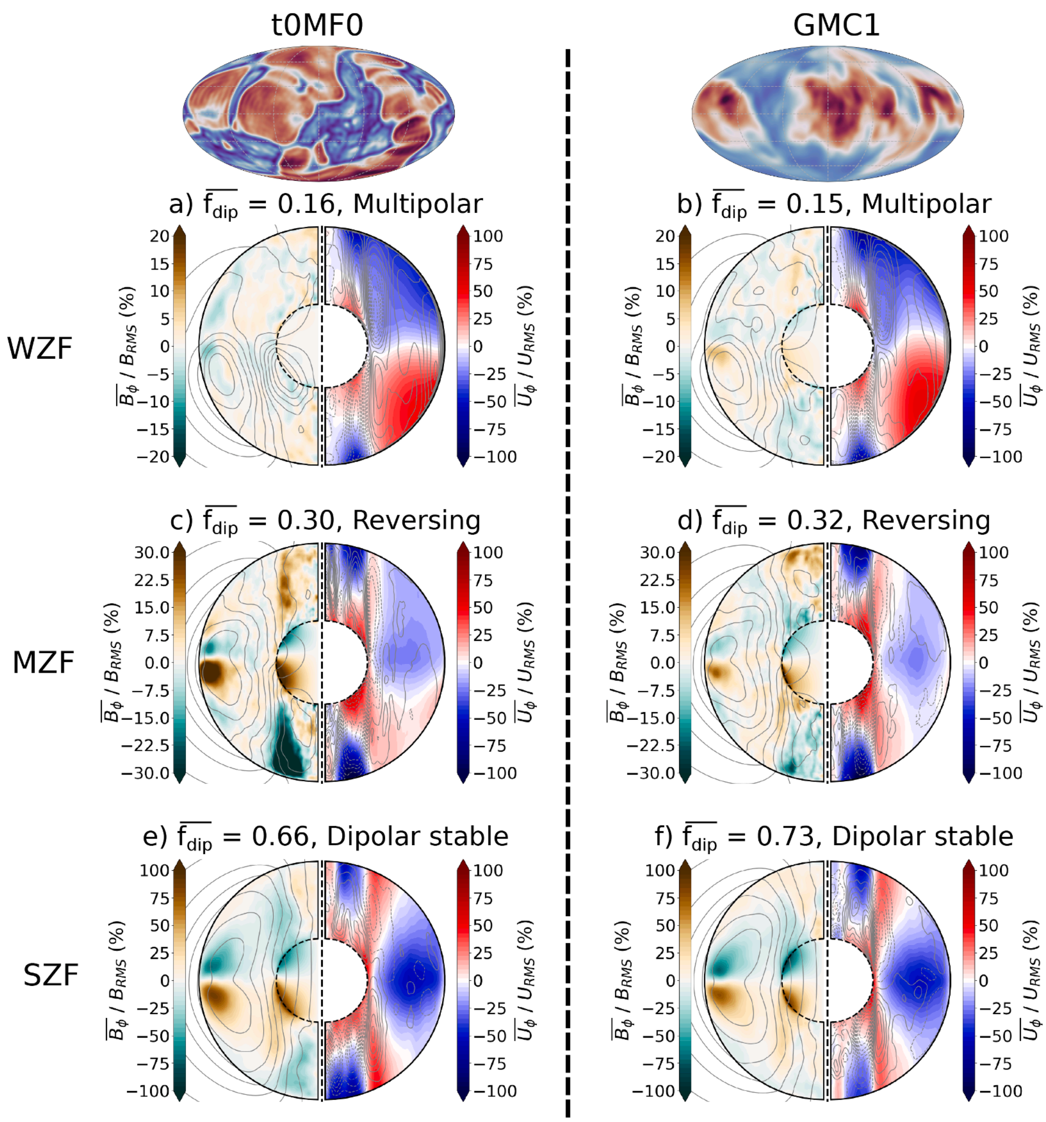

Fig. 4. Meridional cuts showing the azimuthal component of the magnetic field (B_ϕ) and of the velocity (U_ϕ) averaged in time and in the azimuthal direction relative to the root mean square of the fields using the WZF model (Fig. a, b), the MZF model (Fig. c, d) and the SZF model (Fig. e,f). The poloidal field lines are shown as the grey contours. Plain (dashed) field lines represent clockwise (anticlockwise) flows. The amplitude of the heterogeneities are the ones obtained when considering the values in Table 2, i.e. $\delta q_o^* = 4.3$ % for the t0MF0 pattern (Fig. a, c, and e) and $\delta q_o^* = 0.9$ % for the GMC1 pattern (Fig. b, d, and f). Note that the colour scale varies for the magnetic field between the three models. As in Fig. 1, the magnetic field in reversing simulations is multiplied by the sign of the dipole before averaging in time.

patterns are used. The WZF model produces multipolar dynamos, while the SZF model produces strongly dipolar dynamos that do not show the sign of an ability to reverse polarity. The +t0MF0 pattern destabilizes the dipole in the WZF and MZF models despite weakly favouring a polar cooling of the core. This could be caused by the small scale heat flux variations characterizing this pattern, although a more detailed analysis would be required to precisely understand the effect of sharp heat flux variations.

We note that relatively short durations for some simulations make the differentiation between dipolar stable and reversing simulations difficult, and we cannot exclude that dipolar stable simulations would reverse if prolongated long enough.

3.2. Relation between zonal flows and the dipole stability

We show in Fig. 4 the velocity and magnetic field averaged in time and in the azimuthal direction for geodynamo simulations using the +t0MF0 and the +GMC1 patterns. The amplitudes are $\delta q_o^* = 4.3$ % for the t0MF0 pattern and $\delta q_o^* = 0.9$ % for the GMC1 pattern, corresponding to the amplitudes expected when considering the values in Table 2. The time-averaged value of f_{dip} and the behaviour of the dynamo are given at the top for each case. The two dynamos using the WZF model are multipolar (Fig. 4a,b). They are characterized by unstructured small-scale magnetic fields and equatorially antisymmetric zonal flows. Conversely, dynamos using the SZF model are both dipolar and non-reversing. These dipolar stable simulations are characterized by a dominantly dipolar magnetic field and equatorial westward flows (Fig. 4e,f). Westward flows generate azimuthal magnetic field patches of opposite signs near the equator as shown in recent studies (Frasson et al., 2025; Jones and Tsang, 2025). The MZF model produces intermediate dynamos that are dominated by a reversing dipolar magnetic field (Fig. 4c,d). As with the SZF model, equatorial westward flows are found. However, these zonal flows are weaker, and the equatorial symmetry is partially lost with the +t0MF0 pattern. These weaker flows are associated with weaker azimuthal magnetic field patches near the equator.

The patterns effect on the mean fields can be observed when comparing Fig. 4 with Fig. 1. The dipolar stable simulations obtained with

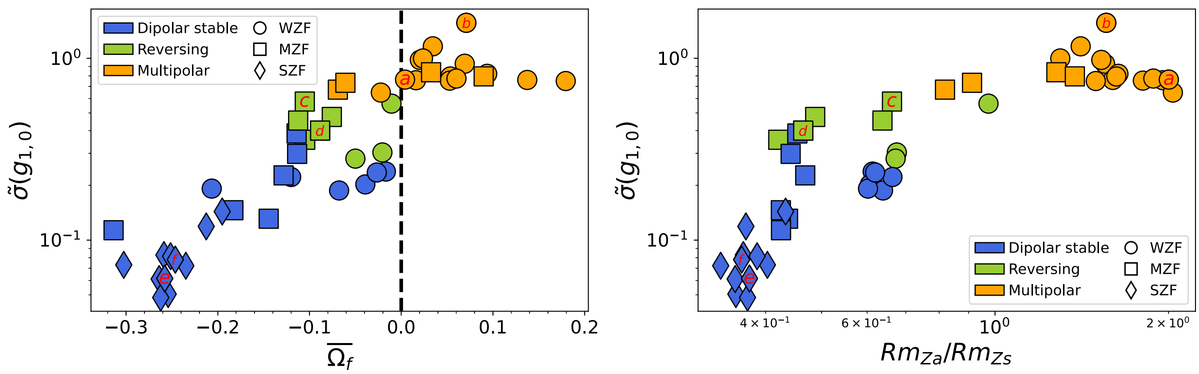

Fig. 5. Fluctuations of the $g_{1,0}$ Gauss coefficient as a function of the mean angular velocity (a) and as a function of the ratio between the zonal antisymmetric and the zonal symmetric flow amplitudes (b). The colour gives the behaviour of the dynamo. The simulations shown in Fig. 4 are labelled a,b,c,d,e, and f.

the SZF model show very little changes in both the magnetic field and the flow, indicating a limited effect of the heat flux heterogeneities on the underlying dynamics. On the contrary, the patterns largely affect the WZF model by disrupting the equatorial westward flow and consequently suppressing the opposite azimuthal flux patches characterizing dipolar simulations. While this is not the focus of this study, the magnetic and velocity fields can significantly vary from the time average, especially during reversals. We notably find that the flow equatorial symmetry is significantly reduced when the dipole is weak in the WZF model, which is not the case in the MZF model (see Fig. A in supplementary).

In order to quantify the variability of the magnetic dipole we compute the fluctuations of the $g_{1,0}$ Gauss coefficient of degree 1 and order 0 defined as $\tilde{\sigma}(g_{1,0}) = \sigma(g_{1,0})/\overline{g_{1,0}}$, where $\sigma(g_{1,0})$ is the standard deviation of $g_{1,0}$. The time average $\overline{g_{1,0}}$ quantifies the axial dipole amplitude, and $\tilde{\sigma}(g_{1,0})$ quantifies its variability. In Fig. 5(a) we show that $\tilde{\sigma}(g_{1,0})$ is relatively well correlated with $\overline{\Omega_f}$. As observed with simpler heat flux geometries (Frasson et al., 2025), reversing dynamos are found for weak and moderate westward flows ($-0.1 \lesssim \overline{\Omega_f} \leq 0$). Only stably dipolar dynamos are found when stronger westward flows exist ($\overline{\Omega_f} \lesssim -0.1$), while only highly variable multipolar dynamos are obtained when eastward flows dominate ($\overline{\Omega_f} \geq 0$). The simulations shown in Fig. 4 are highlighted in Fig. 5. Though multipolar simulations have strong zonal flows (see Fig. 4a,b), these are largely equatorially antisymmetric, causing moderate or small values of $\overline{\Omega_f}$.

As shown in Fig. 5(b), the transition towards unstable multipolar dynamos is also associated with an increase in the equatorial antisymmetry of the zonal flows, quantified by the ratio between the zonal antisymmetric magnetic Reynolds number $\overline{Rm_{Za}}$ and the zonal symmetric magnetic Reynolds number $\overline{Rm_{Zs}}$. This is consistent with the antisymmetry of the mean zonal flows in the multipolar dynamos shown in Fig. 4(a,b). Reversing dynamos have similar or larger amounts of equatorial antisymmetry in the zonal flows compared to dipolar stable dynamos. For instance, we can compare the reversing dynamos shown in Fig. 4(c) and (d). The dynamo in Fig. 4(d) using the MZF model and the +GMC1 pattern shows a strongly equatorially symmetric mean zonal flow, and the value of $\overline{Rm_{Za}}/\overline{Rm_{Zs}}$ is similar to that of the equivalent dipolar stable dynamos obtained with the same model. However, the dynamo in Fig. 4(c) using the same MZF model but the +t0MF0 pattern has an increased antisymmetry in mean zonal flows, and the value of $\overline{Rm_{Za}}/\overline{Rm_{Zs}}$ is increased. A similar transition associated with an increased equatorial antisymmetry has been reported for homogeneous simulations when the forcing of convection is increased above a threshold value (Landeau and Aubert, 2011; Garcia et al., 2017). Here, the same transition is triggered by heat flux heterogeneities without changing the mean convective forcing.

3.3. Control of the dipolar-multipolar transition

We show in Fig. 6(a) the dipolar fraction of the magnetic field at the CMB as a function of the magnetic to kinetic energy ratio within the core. The results of Frasson et al. (2025) from simulations using the same geodynamo models but simpler heat flux geometries are also shown in this figure. The energy ratio was found in previous studies to correlate with the transition between dipolar and multipolar dynamos, with multipolar solutions obtained for $\overline{E_b}/\overline{E_u} \leq 1$ (Tassin et al., 2021). Our models with heterogeneous CMB heat flux conditions show that the transition towards a multipolar behaviour is indeed associated with a decrease of the energy ratio. However, the value of $\overline{E_b}/\overline{E_u}$ at which the transition occurs depends on the numerical model considered.

Frasson et al. (2025) found that the dipolar fraction of the magnetic field correlates better with M^*_{Za} (Eq. (9)). We show in Fig. 6(b) that this correlation holds when more realistic heat flux patterns are used. Simulations with $M^*_{Za} \geq 2 \times 10^{-4}$ are strongly dipolar, while simulations with $M^*_{Za} \leq 2 \times 10^{-5}$ are multipolar. Reversing dynamos are found for intermediate values ($2 \times 10^{-5} \leq M^*_{Za} \leq 2 \times 10^{-4}$). Note that reversing dynamos where found for larger values of M^*_{Za} by Frasson et al. (2025) using a dynamo model not used in this study. Such correlation is expected to some extent. The magnetic dipole has a zonal and equatorially antisymmetric geometry. Strongly dipolar simulations can thus be expected to have large zonal antisymmetric magnetic energies. This effect is reinforced by the strong antisymmetric azimuthal magnetic field patches near the equator in these simulations (Fig. 4e,f). Conversely, zonal flows show a clear equatorial symmetry in dipolar simulations, leading to low values of zonal antisymmetric kinetic energy relative to the zonal symmetric kinetic energy (Fig. 5b). We thus expect strongly dipolar simulations to be characterized by large M^*_{Za}, as we observe. On the contrary, multipolar dynamos have weak dipoles and lack the azimuthal magnetic flux patches, yielding lower zonal antisymmetric magnetic energies. These dynamos have stronger equatorially antisymmetric zonal flows compared to dipolar simulations (Fig. 4a,b), translating into larger zonal antisymmetric kinetic energies (Fig. 5b). Thus, we expect multipolar dynamos to be characterized by low M^*_{Za}. The fact that reversing dynamos are found for intermediate values is consistent with the slight increase in equatorial antisymmetry in the zonal flows (Fig. 5) and the lower dipolar fraction relative to dipolar stable simulations.

Estimating M^*_{Za} for Earth is not straightforward, as the interior flow amplitude and the relative part of the zonal antisymmetric flow and magnetic fields are not well constrained. Nevertheless, Earth's core can be expected to be in the range $7 \times 10^{-5} \leq M^*_{Za} \leq 7 \times 10^{-4}$ (Frasson et al., 2025). This range is highlighted by the grey shaded region in Fig. 6. Our results are consistent with the present-day behaviour of the geodynamo,

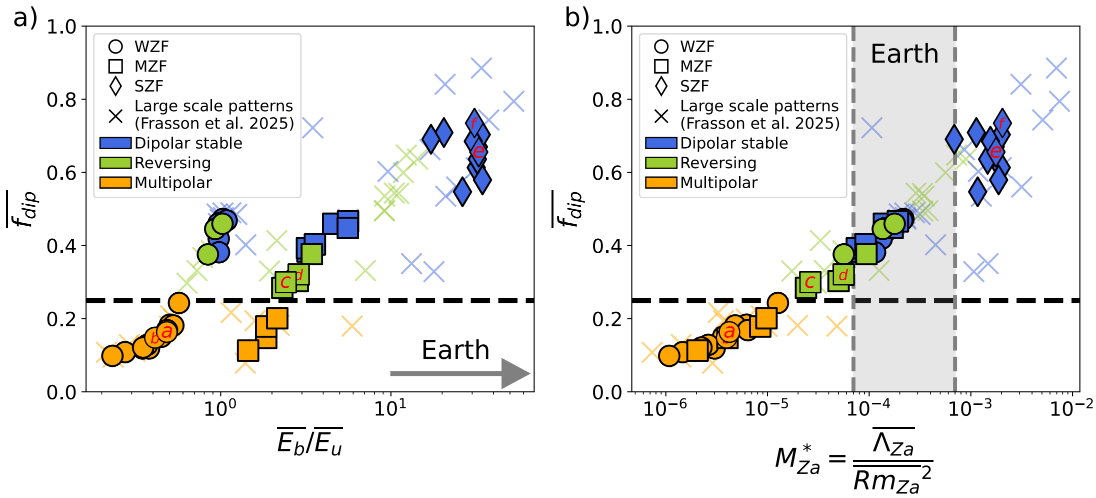

Fig. 6. Dipolar fraction of the magnetic field at the CMB as a function of the magnetic to kinetic energy ratio (a) and as a function of the M^*_{Za} parameter as defined in Eq. (9)(b). Markers correspond to the different geodynamo models. The colour gives the behaviour of the dynamo. The crosses show the data from the geodynamo simulations using large scale patterns from Frasson et al. (2025) (note that these data include results from two extra geodynamo models that have not been used in the present study). The horizontal dashed line at $\overline{f_{dip}} = 0.25$ demarcates the dipolar simulations (above) from the multipolar simulations (below). The grey shaded area shows the expected range of values of M^*_{Za} for the Earth. The simulations shown in Fig. 4 are labelled a,b,c,d,e, and f.

as we find dipolar stable and reversing dynamos within this range. We note that previously suggested criteria reported as controlling parameters of the dipolar/multipolar transition in numerical simulations of the geodynamo such as the local Rossby number (Christensen and Aubert, 2006) and the kinetic to magnetic energy ratio (Tassin et al., 2021) predict a strongly dipolar non-reversing dynamo at present day. The M^*_{Za} parameter enables us to solve this discrepancy, as reversing dynamos are found in the range expected for the present-day Earth.

4. Discussion

4.1. Sensitivity of geodynamo models to heat flux heterogeneities

We find that the heat flux pattern representative of the present-day (+t0MF0) is destabilizing the magnetic dipole in the WZF model. The two models with stronger zonal flows are not significantly affected by this pattern. Although the +t0MF0 pattern is slightly different from the tomographic pattern, some important characteristics, such as the dominance of the $Y_{2,2}$ component and the lower equatorial heat flux, are shared. Several studies found that the tomographic pattern destabilizes the magnetic dipole (Olson et al., 2010; Olson and Amit, 2014), consistent with the effect of the +t0MF0 pattern on the WZF model. More recent results nevertheless suggest that the tomographic pattern could stabilize the dipole for large heterogeneity amplitudes (Mound and Davies, 2023; Terra-Nova and Amit, 2024). This effect was not observed in our simulations possibly because the spherically averaged CMB heat flux is isentropic in our models, whereas a super-isentropic heat flux is imposed at the CMB in most other studies.

We find, however, that the effect of a given pattern, and particularly the present-day pattern, is significant only when zonal flows are weak. We note that Kutzner and Christensen (2004) also did not observe a destabilization of the dipole when using the tomographic pattern, consistent with the results we obtain using models with larger zonal flows (MZF and SZF). This model dependence of the effect of the tomographic pattern together with the non-monotonous effect of the heterogeneity pattern when increasing its amplitude demonstrates the difficulty to precisely understand the role of heat flux heterogeneities, even in the present-day dynamo process.

These results suggest that the sensitivity of geodynamo models to heat flux heterogeneities can be a way to discriminate simulations that can reproduce the present and past behaviour of the geodynamo. For example, our WZF model cannot sustain a strong dipole when adding the +t0MF0 pattern, showing its inability to produce a dipolar solution for present-day conditions. Only a strongly dominant polar cooling of the core (as is the case for the -GMC1 pattern) allows the WZF model to maintain a strong dipole, suggesting that such a model would predict a multipolar dynamo for most of the life time of the geodynamo. The SZF model, on the contrary, only produces stable polarity periods. Although reversals could eventually occur, the SZF model is unlikely to allow frequent reversals as observed during the Jurassic (Gallet and Pavlov, 2016), the Carboniferous (Hounslow et al., 2024), or the Ediacarian-Cambrian transition (Shen et al., 2025), even if a strong equatorial cooling is favoured as with the GMC1 pattern. The MZF model allows a strong and reversing dipole with the present-day heat flux pattern, but it also allows variations in the dipole stability depending notably on the dominance of equatorial or polar cooling. Models with moderate zonal flows are, thus, the most likely to allow variations in the reversal frequency induced by variations in the lower mantle thermal conditions. Hence, our results suggest that moderate zonal flow models should be preferred to study the effect on the geodynamo of a changing heat flux heterogeneity at the CMB.

4.2. Dominance of equatorial versus polar cooling

Using positive and negative amplitudes for the t0MF0 and GMC1 patterns enables us to assess to what extent the effect of the pattern depends on whether polar or equatorial cooling is favoured. It emerges from our results that patterns even weakly favouring an equatorial cooling of the core are the most efficient at destabilizing the dipole. We systematically obtain a multipolar behaviour for smaller amplitudes of the patterns when an equatorial cooling is favoured compared to when a polar cooling is favoured. This is consistent with previous studies showing that a pure equatorial cooling of the core strongly destabilizes the dipole (Kutzner and Christensen, 2004; Olson et al., 2010; Frasson et al., 2025). Here, we further show that the equatorial cooling does not need to be strongly dominant for this effect to occur. This supports the common approach of assuming that larger equatorial heat fluxes in the past caused by equatorial subductions are related to larger reversal frequencies (Biggin et al., 2012; Dannberg et al., 2024).

Importantly, however, the extent to which the dipole can be destabilized is highly dependent on the geodynamo model considered. Our results suggest that a dominant equatorial cooling of the core starts significantly destabilizing the dipole only when westward flows are substantially weakened by thermal winds induced by the equatorial cooling. For this reason, the SZF model is essentially unaffected by the two considered patterns regardless of the amplitude and sign because zonal flows are too strong to be overcome by the induced thermal winds. Frasson et al. (2025) showed that the SZF model eventually reverses polarity when stronger equatorial coolings are considered, with amplitudes equivalent to $\left[\delta q_o^*\right]_{2,0} \lesssim -5.2\,\%$. Such large amplitudes of the degree 2 order 0 component would require heterogeneity amplitudes much larger than the ones expected considering the values in Table 2.

4.3. Weak zonal flow reversals

Our geodynamo simulations produce magnetic reversals when zonal flows are weak outside the tangent cylinder, or strongly equatorially antisymmetric. Inertia is thought to be responsible for most reversing dynamos, with reversals occurring when $E_b/E_u \sim 1$ (Tassin et al., 2021). This applies to our WZF model, which reverses only when $E_b/E_u \lesssim 1$. Although the energy ratio is slightly larger with the MZF model, reversals occur for $E_b/E_u \simeq 2$, suggesting that inertia could still play a role in the reversing mechanism. Recent studies show that reversals can be obtained in numerical simulations without the need for a strong inertia, either by increasing the Prandtl number (Jones and Tsang, 2025), or by imposing a stratification at the top of the core in bottom-driven dynamos (Aubert et al., 2025). Our models do not follow these paths, and more studies are required to investigate these new reversing mechanisms. We note, nevertheless, that Frasson et al. (2025) found reversing dynamos despite $E_b/E_u \sim 10$ with a pure equatorial cooling of the core using a numerical model with even stronger zonal flows than the SZF used here. As the SZF model is not affected by the patterns used in this study, we also do not expect any effect of these patterns on this even more extreme model.

This precaution put aside, it is noteworthy that reversing dynamos obtained by Jones and Tsang (2025) have vanishing westward equatorial flows and homogenized temperatures in the core when using $Pr > 1$. The reversing dynamos obtained in our study share these characteristics. Here, zonal flows are suppressed through the boundary heat flux rather than through an increase in the Peclet number. The weakening of these zonal flows implies the subsequent weakening of the azimuthal magnetic flux patches on either side of the equator. As hypothesised by Jones and Tsang (2025), the existence of these azimuthal flux patches could favour the production of a poloidal magnetic field of the same polarity as the ambient dipole, reinforcing its stability. In this view, zonal flows could help strengthening and stabilizing the dipole. Our results show that such stabilization of the magnetic dipole could also occur in $Pr = 1$ models otherwise prone to reversals when zonal flows are weakened. This suggests that zonal flows could be responsible for a reinforced stability of the dipole in a broad range of dynamo models. Similar results have been obtained in the context of Saturn (Stanley, 2010; Yan and Stanley, 2021), for which strong westward flows have been suggested as a way to produce the observed highly axisymmetric dipole. We stress that vanishing zonal flows are not a sufficient condition to obtain reversals, as dipolar stable solutions exist despite weak zonal flows (see Fig. 5). It seems, however, that such condition facilitates their occurrence.

Moreover, zonal flows are coupled to the meridional circulation. The suppression of azimuthal flows can thus be associated with a change in the meridional circulation, which could also affect the dipole generation mechanism. Aubert et al. (2025) showed that applying a global stratification at the top of the core can cause reversals. They associate the occurrence of reversals to the weakening of equatorial upwellings. Interestingly, an equatorial cooling of the core also weakens upwellings through the weakening of the meridional circulation. Thus, it is possible that a mechanism similar to the one suggested by Aubert et al. (2025) is at play in equatorially cooled dynamos. Furthermore, the simulations in this study have an isentropic heat flux at the top of the core on average, causing local stratifications under low heat flux regions. In the case of a preferred equatorial cooling, the stratification exists mostly inside the tangent cylinder, while the equatorial region is convectively unstable.

We find that the magnetic field dipolarity at the CMB is well correlated with M^*_{Za}, which can be understood as a quantification of the dipole strength relative to the strength of the equatorially antisymmetric zonal flows. This parameter better separates dipolar and multipolar dynamos than the magnetic to kinetic energy ratio previously suggested (Tassin et al., 2021), highlighting the importance of equatorial antisymmetry in the dipolar-multipolar transition. Only multipolar and only non-reversing dynamos are found for the lowest and largest values, respectively. Crucially, reversals are obtained for a range of values ($2 \times 10^{-5} \leq M^*_{Za} \leq 2 \times 10^{-4}$) that overlaps the estimates in Earth's core ($7 \times 10^{-5} \leq M^*_{Za} \leq 7 \times 10^{-4}$). As reversing dynamos obtained by Jones and Tsang (2025) share the characteristics highlighted in this study (e.g. vanishing westward flows and azimuthal magnetic flux patches), it can be reasonably expected for M^*_{Za} to show a similar correlation with $\overline{f_{dip}}$ and the dynamo behaviour in the high Pr regime. Reversals induced by a global stratification at the top of the core (i.e. Aubert et al., 2025) are also controlled by the temperature distribution, although homogeneous across the CMB, and the potential relevance of M^*_{Za} in this case remains to be shown. The correlation between f_{dip} and M^*_{Za} is partially explained by the numerator of M^*_{Za} that mostly quantifies the dipole amplitude. However, the denominator significantly improves the correlation, highlighting the role of the equatorial symmetry.

4.4. Past behaviour of the geodynamo

Though only two heat flux patterns have been used in this study, our results show, as discussed in Section 4.2, that the dominance of equatorial or polar cooling of the core is controlling to a large extent the stability of the dipole when the top of the core is isentropic on average. Thus, we can compare the evolution of the degree 2 order 0 component of the CMB heat flux in the Earth's past with the reversal frequency of the magnetic field reflecting the dipole stability.

Of the 6 mantle convection cases presented in Frasson et al. (2024), the MF* case is the most likely to show a realistic evolution of the CMB heat flux as it is given in a paleomagnetic reference frame. This MF* case displays a sharp change from a strongly dominant polar cooling to a strongly dominant equatorial cooling a few Myr before the start of the Devonian around 430 Ma due to fast true polar wander (see Fig. 8 in Frasson et al. (2024)). The strong polar cooling prior to the Devonian is consistent with the period of dipole stability during the Ordovician superchron (490 Ma – 460 Ma) (Pavlov and Gallet, 2005). A strongly dominant equatorial cooling persists for the whole of the Devonian (420 Ma – 359 Ma), and starts to decrease after 340 Ma. There is strong evidence that the Devonian was a period of hyperactivity for the magnetic field, indicating that the dipole might have been weaker and less stable at this time (Shcherbakova et al., 2017; Hawkins et al., 2019; van der Boon et al., 2022). These observations are consistent with the dominant equatorial cooling predicted by the MF* case for this period. In contrast, other models predict a minimum in the equatorial heat flux around 400 Ma (Zhang and Zhong, 2011; Dannberg et al., 2024). However, this comparison has to be made with care, as the metrics employed are different (amplitude of the degree 2 order 0 component in Frasson et al. (2024) and total equatorial heat flux in Zhang and Zhong (2011) and Dannberg et al. (2024)). Similarly, Zhang and Zhong (2011) found equatorial heat flux minima correlating with the Kiaman superchron (316 – 262 Ma) and the Cretaceous superchron (125 – 83 Ma). However, these equatorial heat flux minima are less clear in the models from Dannberg et al. (2024) and in the MF* case (Frasson et al., 2024). Moreover, Choblet et al. (2016) showed that lower reversal frequencies tend to be associated with larger equatorial cooling over the past 160 Ma, suggesting that the Cretaceous superchron has not been caused by increased polar cooling.

We stress that such comparisons are very tentative, as heat flux reconstructions this deep in time are probably lacking accuracy, notably due to uncertainties in the plate reconstructions prior to the Pangea assembly (Seton et al., 2023). It is also known that heat flux geometries other than the degree 2 order 0 such as an equatorial antisymmetric heat flux can lead to a destabilization of the dipole (Glatzmaier et al., 1999; Frasson et al., 2025). Moreover, significant changes in the geodynamo behaviour can have other sources than the boundary condition, such as the nucleation of the inner core and variations in the convective power (Driscoll, 2016). These changes would affect the boundary conditions and the basic state. Their effect on the reversal dynamics can't be deduced from our study, where we have a strong buoyancy flux at the inner-core boundary and isentropic conditions at the top (see e.g. Aubert et al., 2025, for other choices). Nevertheless, the correlations highlighted in this study do not explicitly depend on such choices, and future studies are needed to evaluate whether their relevance is specific or if they apply to a broad range of models.

5. Conclusion

We conducted geodynamo simulations with two heat flux patterns derived from mantle convection models. Varying the amplitude and sign of the patterns, we find that the dominance of equatorial or polar cooling of the core is a key factor affecting the stability of the dipole. A dominant equatorial cooling favours unstable dipoles and vice versa. However, we showed that the effect of a given pattern depends on the underlying geodynamo model. Models with strong westward flows are less affected by heterogeneous heat flux patterns, while reversing dynamos are found for weak westward flows. This supports previous findings that reducing the amplitude of zonal flows can help obtain reversals (Frasson et al., 2025; Jones and Tsang, 2025). The parameter M^*_{Za} is found to correlate well with the dipolar fraction of the magnetic field when realistic CMB heat flux patterns are used, generalizing the results obtained by Frasson et al. (2025).

These results strengthen the claim that the observed reversal frequency variations could reflect, to some extent, variations in the amplitude of the equatorial heat flux relative to higher latitudes. Several other parameters known to affect the dipole stability are not considered explicitly in this study, such as the total heat flux at the CMB or the inner core size. However, those parameters are expected to vary on long time scales controlled by the secular cooling of the Earth and mantle convection. To some extent, the three dynamical states we have considered (WZF, MZF and SZF) represent an attempt to account for the poorly known, long time-scale evolution of the core. On the other hand, lateral contrasts in heat flux considered here can vary non-monotonically and on shorter time scales due to true polar wander (Frasson et al., 2024). We showed that the heat flux patterns considered in this study act mostly through the contrast between the poles and the equator, even when this contrast is small. Although our patterns are not equatorially symmetric, the level of symmetry breaking they impose to the core seems to have a secondary effect on the dipole reversal frequency. Changes on longer time scales in the total CMB heat flux and inner core size are unlikely to trigger fast regime changes of the geodynamo. However, these changes can gradually affect the sensitivity of the geodynamo to heat flux heterogeneities through geological times.

CRediT authorship contribution statement

T. Frasson: Writing – original draft, Visualization, Investigation, Formal analysis, Data curation, Conceptualization; **N. Schaeffer:** Writing – review & editing, Software, Investigation, Funding acquisition, Conceptualization; **H.-C. Nataf:** Writing – review & editing, Supervision, Investigation, Conceptualization; **S. Labrosse:** Writing – review & editing, Supervision, Investigation, Conceptualization.

Data availability

The *XSHELLS* code used to run the geodynamo simulations is freely available at https://nschaeff.bitbucket.io/xshells/.

Declaration of competing interest

The authors declare that they have no known competing financial interests or personal relationships that could have appeared to influence the work reported in this paper.

Acknowledgement

This research has been supported by the Agence Nationale de la Recherche (grant no. ANR-19-CE31-0019). Numerical simulations have been performed using HPC resources of IDRIS, TGCC and CINES under allocations A0100407382, A0120407382, A0140407382 and A0160407382 attributed by GENCI (Grand Equipement National de Calcul Intensif). The XSHELLS code received funding from the European High-Performance Computing Joint Undertaking (JU) under Grant Agreement No 101093038 (ChEESE-2P).

Supplementary material

Supplementary material associated with this article can be found in the online version at 10.1016/j.epsl.2026.120089.

Appendix A. Simulation details

We give in Tables A.1, A.2, and A.3 the outputs for the geodynamo simulations used in this study.

Table A.1
Outputs from simulations using the WZF model. The types are DS for dipolar stable, R for reversing, and M for multipolar.

Pattern	δq^*_o (%)	Δt_{sim} (t_d)	$\overline{f_{dip}}$	$\overline{M^*_{Za}}$ ($\times 10^{-4}$)	$\overline{\frac{E_b}{E_u}}$	$\overline{Rm}$	$\overline{\Lambda}$	$\overline{\Omega_f}$ (%)	Type
—	0.00	134.3	0.45	1.36	0.95	649	13.11	-2.1	R
t0MF0	-0.36	30.2	0.17	0.06	0.5	703	8.0	3.4	M
t0MF0	-0.71	30.7	0.24	0.13	0.6	692	9.12	2.4	M
t0MF0	-1.43	29.9	0.12	0.03	0.38	726	6.7	5.4	M
t0MF0	-3.57	30.0	0.13	0.03	0.38	736	6.7	5.3	M
t0MF0	-5.71	30.3	0.12	0.02	0.36	749	6.57	6.0	M
t0MF0	0.36	31.9	0.46	1.8	0.99	646	13.56	-2.7	DS
t0MF0	0.71	31.4	0.38	0.56	0.88	659	12.26	-1.1	R
t0MF0	1.43	29.9	0.18	0.06	0.52	700	8.25	2.0	M
t0MF0	3.57	29.5	0.15	0.04	0.46	714	7.64	1.6	M
t0MF0	4.28	29.4	0.16	0.04	0.49	709	8.13	0.4	M
t0MF0	5.71	29.7	0.18	0.05	0.54	705	8.77	-2.2	M
GMC1	-0.32	31.6	0.47	2.17	1.05	640	14.17	-3.9	DS
GMC1	-0.65	31.4	0.46	1.78	1.05	640	14.06	-5.0	M
GMC1	-1.30	31.7	0.47	2.12	1.1	632	14.5	-6.8	DS
GMC1	-3.24	31.0	0.42	1.33	0.99	635	13.14	-12.0	DS
GMC1	-5.19	30.5	0.38	1.14	0.99	632	13.05	-20.7	DS
GMC1	0.32	31.6	0.44	1.56	0.95	650	13.18	-1.7	DS
GMC1	0.65	30.1	0.12	0.03	0.38	731	6.74	6.9	M
GMC1	0.91	29.1	0.15	0.04	0.43	727	7.29	7.1	M
GMC1	1.30	29.9	0.12	0.02	0.35	746	6.49	9.4	M
GMC1	3.24	30.1	0.11	0.01	0.28	789	5.72	13.7	M
GMC1	5.19	30.6	0.10	0.01	0.23	826	5.27	17.9	M

Table A.2
Same as in A.1 for MZF.

Pattern	δq_o^* (%)	Δt_{sim} (t_d)	$\overline{f_{dip}}$	$\overline{M^*_{Za}}$ ($\times 10^{-4}$)	$\overline{\frac{E_b}{E_u}}$	$\overline{Rm}$	$\overline{\Lambda}$	$\overline{\Omega_f}$ (%)	Type
—	0.00	96.0	0.38	0.94	3.49	987	16.78	-10.5	R
t0MF0	-1.43	6.0	0.40	0.92	3.64	984	17.36	-11.4	DS
t0MF0	-3.57	3.2	0.18	0.08	1.89	1075	10.73	-6.9	M
t0MF0	-5.71	6.0	0.20	0.1	2.22	1074	12.45	-6.1	M
t0MF0	1.43	6.0	0.38	0.79	3.32	997	16.14	-11.4	DS
t0MF0	3.57	3.2	0.39	0.76	3.27	1004	16.23	-12.8	DS
t0MF0	4.28	5.4	0.30	0.26	2.52	1045	13.24	-10.5	R
t0MF0	5.71	8.7	0.28	0.24	2.37	1053	12.8	-11.2	R
GMC1	-1.30	3.3	0.46	1.4	4.63	946	20.57	-14.4	DS
GMC1	-3.24	2.8	0.47	1.92	5.67	919	23.74	-18.3	DS
GMC1	-5.19	2.1	0.45	1.7	5.65	931	24.25	-31.4	DS
GMC1	0.91	9.3	0.32	0.56	2.92	1013	14.76	-8.8	R
GMC1	1.30	4.0	0.30	0.5	2.9	1017	14.71	-7.6	R
GMC1	3.24	3.2	0.15	0.04	1.94	1126	11.8	3.3	M
GMC1	5.19	3.0	0.11	0.02	1.54	1202	10.54	9.0	M

Table A.3
Same as in A.1 for SZF.

Pattern	δq_o^* (%)	Δt_{sim} (t_d)	$\overline{f_{dip}}$	$\overline{M^*_{Za}}$ ($\times 10^{-4}$)	$\overline{\frac{E_b}{E_u}}$	$\overline{Rm}$	$\overline{\Lambda}$	$\overline{\Omega_f}$ (%)	Type
—	0.00	5.1	0.61	19.92	32.12	399	16.92	-23.5	DS
t0MF0	-3.57	3.2	0.70	19.91	34.5	393	17.57	-25.9	DS
t0MF0	-5.71	3.3	0.69	15.57	31.02	405	16.75	-25.2	DS
t0MF0	3.57	3.0	0.67	17.36	33.08	397	17.29	-26.2	DS
t0MF0	4.28	3.6	0.66	17.66	33.28	396	17.26	-25.8	DS
t0MF0	5.71	3.0	0.64	14.62	32.73	403	17.54	-30.3	DS
GMC1	-3.24	2.9	0.58	18.76	35.05	398	18.28	-25.4	DS
GMC1	-5.19	2.2	0.55	11.67	26.61	425	15.95	-26.4	DS
GMC1	0.91	2.7	0.73	20.46	31.55	395	16.21	-24.6	DS
GMC1	3.24	3.7	0.71	11.34	20.82	434	12.95	-21.3	DS
GMC1	5.19	2.3	0.69	6.87	17.6	452	11.8	-19.5	DS

References

Amit, H., Choblet, G., 2009. Mantle-driven geodynamo features-effects of post-perovskite phase transition. Earth Planets Space 61, 1255–1268. https://doi.org/10.1186/BF03352978

Amit, H., Choblet, G., Olson, P., Monteux, J., Deschamps, F., Langlais, B., Tobie, G., 2015a. Towards more realistic core-mantle boundary heat flux patterns: a source of diversity in planetary dynamos. Prog. Earth Planet. Sci. 2 (1), 26. https://doi.org/10.1186/s40645-015-0056-3

Amit, H., Deschamps, F., Choblet, G., 2015b. Numerical dynamos with outer boundary heat flux inferred from probabilistic tomography-consequences for latitudinal distribution of magnetic flux. Geophys. J. Int. 203 (2), 840–855. https://doi.org/10.1093/gji/ggv332

Aubert, J., 2023. State and evolution of the geodynamo from numerical models reaching the physical conditions of Earth's core. Geophys. J. Int. 235 (1), 468–487. https://doi.org/10.1093/gji/ggad229

Aubert, J., Finlay, C.C., Fournier, A., 2013. Bottom-up control of geomagnetic secular variation by the Earth's inner core. Nature 502 (7470), 219–223. https://doi.org/10.1038/nature12574

Aubert, J., Gastine, T., Fournier, A., 2017. Spherical convective dynamos in the rapidly rotating asymptotic regime. J. Fluid Mech. 813, 558–593. https://doi.org/10.1017/jfm.2016.789

Aubert, J., Landeau, M., Fournier, A., Gastine, T., 2025. Core-surface kinematic control of polarity reversals in advanced geodynamo simulations. Phys. Earth Planet. Int., 107365. https://doi.org/10.1016/j.pepi.2025.107365

Biggin, A.J., Steinberger, B., Aubert, J., Suttie, N., Holme, R., Torsvik, T.H., van der Meer, D.G., van Hinsbergen, D. J.J., et al., 2012. Possible links between long-term geomagnetic variations and whole-mantle convection processes. Nat. Geosci. 5 (8), 526–533. https://doi.org/10.1038/ngeo1521

van der Boon, A., Biggin, A.J., Thallner, D., Hounslow, M.W., Bono, R., Nawrocki, J., Wójcik, K., Paszkowski, M., Königshof, P., de Backer, T., et al., 2022. A persistent non-uniformitarian paleomagnetic field in the devonian? Earth Sci. Rev. 231, 104073. https://doi.org/10.1016/j.earscirev.2022.104073

Braginsky, S.I., Roberts, P.H., 1995. Equations governing convection in Earth's core and the geodynamo. Geophys. Astrophys. Fluid Dyn. 79 (1–4), 1–97. https://doi.org/10.1080/03091929508228992

Choblet, G., Deschamps, F., Amit, H., Lasbleis, M., 2023. Inferring the relationship between core-mantle heat flux and seismic tomography from mantle convection simulations. PEPI 342, 107072. https://doi.org/10.1016/j.pepi.2023.107072

Choblet, G., Hagay, A., Husson, L., 2016. Constraining mantle convection models with palaeomagnetic reversals record and numerical dynamos. Geophys. J. Int. 207 (2), 1165–1184. https://doi.org/10.1093/gji/ggw328

Christensen, U.R., Aubert, J., 2006. Scaling properties of convection-driven dynamos in rotating spherical shells and application to planetary magnetic fields. Geophys. J. Int. 166 (1), 97–114. https://doi.org/10.1111/j.1365-246X.2006.03009.x

Cottaar, S., Lekic, V., 2016. Morphology of seismically slow lower-mantle structures. Geophys. J. Int. 207 (2), 1122–1136. https://doi.org/10.1093/gji/ggw324

Cox, A., Doell, R.R., Dalrymple, G.B., 1964. Reversals of the Earth's magnetic field. Science 144 (3626), 1537–1543. https://doi.org/10.1126/science.144.3626.1537

Dannberg, J., Gassmoeller, R., Thallner, D., LaCombe, F., Sprain, C., 2024. Changes in core-mantle boundary heat flux patterns throughout the supercontinent cycle. Geophys. J. Int. , 1251–1274. https://doi.org/10.1093/gji/ggae075

Davies, C.J., 2015. Cooling history of Earth's core with high thermal conductivity. Phys. Earth Planet. Int. 247, 65–79. https://doi.org/10.1016/j.pepi.2015.03.007

Dormy, E., 2016. Strong-field spherical dynamos. J. Fluid Mech. 789, 500–513. https://doi.org/10.1017/jfm.2015.747

Driscoll, P.E., 2016. Simulating 2 ga of geodynamo history. Geophys. Res. Lett. 43 (11), 5680–5687. https://doi.org/10.1002/2016GL068858

Durand, S., Debayle, E., Ricard, Y., Zaroli, C., Lambotte, S., 2017. Confirmation of a change in the global shear velocity pattern at around 1000 km depth. Geophys. J. Int. 211 (3), 1628–1639. https://doi.org/10.1093/gji/ggx405

Frasson, T., Labrosse, S., Nataf, H.-C., Coltice, N., Flament, N., 2024. On the impact of true polar wander on heat flux patterns at the core–mantle boundary. Solid Earth 15 (5), 617–637. https://doi.org/10.5194/se-15-617-2024

Frasson, T., Schaeffer, N., Nataf, H.C., Labrosse, S., 2025. Geomagnetic dipole stability and zonal flows controlled by mantle heat flux heterogeneities. Geophys. J. Int. 240 (3), 1481–1504.

Gallet, Y., Pavlov, V.E., 2016. Three distinct reversing modes in the geodynamo. Izv., Phys. Solid Earth 52 (2), 291–296. https://doi.org/10.1134/S106935131602004X

Garcia, F., Oruba, L., Dormy, E., et al., 2017. Equatorial symmetry breaking and the loss of dipolarity in rapidly rotating dynamos. Geophys. Astrophys. Fluid Dyn. 111 (5), 380–393. https://doi.org/10.1080/03091929.2017.1347785

Glatzmaier, G.A., Coe, R.S., Hongre, L., Roberts, P.H., 1999. The role of the Earth's mantle in controlling the frequency of geomagnetic reversals. Nature 401 (6756), 885–890. https://doi.org/10.1038/44776

Guervilly, C., Cardin, P., Schaeffer, N., 2019. Turbulent convective length scale in planetary cores. Nature 570 (7761), 368–371. https://doi.org/10.1038/s41586-019-1301-5

Hawkins, L., Anwar, T., Shcherbakova, V.V., Biggin, A.J., Kravchinsky, V.A., Shatsillo, A.V., Pavlov, V.E., 2019. An exceptionally weak devonian geomagnetic field recorded by the viluy traps, siberia. Earth Planet. Sci. Lett. 506, 134–145. https://doi.org/10.1016/j.epsl.2018.10.035

Hounslow, M.W., Biggin, A.J., Cózar, P., Somerville, I.D., Kamenikova, T., Sprain, C.J., 2024. A hyperactive geomagnetic field in the late visean (early carboniferous) from the late asbian stratotype section in northwest england, UK. Geochem. Geophys. Geosyst. 25 (4), e2023GC011282. https://doi.org/10.1029/2023GC011282

Jones, C.A., Tsang, Y.-K., 2025. Low inertia reversing geodynamos. Phys. Earth Planet. Int. 360, 107303. https://doi.org/10.1016/j.pepi.2024.107303

Kutzner, C., Christensen, U.R., 2004. Simulated geomagnetic reversals and preferred virtual geomagnetic pole paths. Geophys. J. Int. 157 (3), 1105–1118. https://doi.org/10.1111/j.1365-246X.2004.02309.x

Labrosse, S., 2015. Thermal evolution of the core with a high thermal conductivity. Phys. Earth Planet. Inter. 247, 36–55. https://doi.org/10.1016/j.pepi.2015.02.002

Landeau, M., Aubert, J., 2011. Equatorially asymmetric convection inducing a hemispherical magnetic field in rotating spheres and implications for the past martian dynamo. PEPI 185 (3–4), 61–73. https://doi.org/10.1016/j.pepi.2011.01.004

Lin, Y., Marti, P., Jackson, A., 2025. Invariance of dynamo action in an early-Earth model. Nature , 1–6. https://doi.org/10.1038/s41586-025-09334-y

Lister, J.R., Buffett, B.A., 1995. The strength and efficiency of thermal and compositional convection in the geodynamo. Phys. Earth Planet. Inter. 91 (1–3), 17–30.

Lowrie, W., Kent, D.V., 2004. Geomagnetic polarity timescales and reversal frequency regimes. Timescales Paleomagnetic Field Geophys. Monogr. Ser. 145, 117–129. https://doi.org/10.1029/145GM09

Masters, T.G., Johnson, S., Laske, G., Bolton, H., 1996. A shear-velocity model of the mantle. Philos. Transact. A Math. Phys. Eng. Sci. 354 (1711), 1385–1411.

Merdith, A.S., Collins, A.S., Williams, S.E., Pisarevsky, S., Foden, J.D., Archibald, D.B., Blades, M.L., Alessio, B.L., Armistead, S., Plavsa, D., et al., 2017. A full-plate global reconstruction of the neoproterozoic. Gondwana Res. 50, 84–134. https://doi.org/10.1016/j.gr.2017.04.001

Mound, J., Davies, C., Rost, S., Aurnou, J., et al., 2019. Regional stratification at the top of Earth's core due to core–mantle boundary heat flux variations. Nat. Geosci. 12 (7), 575–580. https://doi.org/10.1038/s41561-019-0381-z

Mound, J.E., Davies, C.J., 2023. Longitudinal structure of earth's magnetic field controlled by lower mantle heat flow. Nat. Geosci. 16 (4), 380–385. https://doi.org/10.1038/s41561-023-01148-9

Nakagawa, T., Tackley, P.J., 2008. Lateral variations in CMB heat flux and deep mantle seismic velocity caused by a thermal-chemical-phase boundary layer in 3D spherical convection. Earth Planet. Sci. Lett. 271 (1–4), 348–358. https://doi.org/10.1016/j.epsl.2008.04.013

Nataf, H.-C., Schaeffer, N., 2024. Dynamic regimes in planetary cores: τ–l diagrams. C. R. Géosci. 356 (G1), 1–30. https://doi.org/10.5802/crgeos.256

Nimmo, F., 2015. 8.02 - Energetics of the core. In: Schubert, G. (Ed.), Treatise on Geophysics (Second Edition). Elsevier, Oxford, pp. 27–55. https://doi.org/10.1016/B978-0-444-53802-4.00139-1

Olson, P., 2015. 8.01 - Core dynamics: an introduction and overview. In: Schubert, G. (Ed.), Treatise on Geophysics (Second Edition). Elsevier, Oxford, pp. 1–25. https://doi.org/10.1016/B978-0-444-53802-4.00137-8

Olson, P., Amit, H., 2014. Magnetic reversal frequency scaling in dynamos with thermochemical convection. Phys. Earth Planet. Int. 229, 122–133. https://doi.org/10.1016/j.pepi.2014.01.009

Olson, P., Deguen, R., Hinnov, L.A., Zhong, S., et al., 2013. Controls on geomagnetic reversals and core evolution by mantle convection in the Phanerozoic. Phys. Earth Planet. Int. 214, 87–103. https://doi.org/10.1016/j.pepi.2012.10.003

Olson, P.L., Coe, R.S., Driscoll, P.E., Glatzmaier, G.A., Roberts, P.H., 2010. Geodynamo reversal frequency and heterogeneous core-mantle boundary heat flow. Phys. Earth Planet. Int. 180 (1–2), 66–79. https://doi.org/10.1016/j.pepi.2010.02.010

Pavlov, V., Gallet, Y., 2005. A third superchron during the early paleozoic. Epis. J. Int. Geosci. 28 (2), 78–84.

Sahoo, S., Sreenivasan, B., Amit, H., 2016. Dynamos driven by weak thermal convection and heterogeneous outer boundary heat flux. Phys. Earth Planet. Int. 250, 35–45. https://doi.org/10.1016/j.pepi.2015.11.003

Schaeffer, N., Jault, D., Nataf, H.-C., Fournier, A., 2017. Turbulent geodynamo simulations: a leap towards Earth's core. Geophys. J. Int. 211 (1), 1–29. https://doi.org/10.1093/gji/ggx265

Seton, M., Williams, S.E., Domeier, M., Collins, A.S., Sigloch, K., 2023. Deconstructing plate tectonic reconstructions. Nat. Rev. Earth Environ. 4 (3), 185–204. https://doi.org/10.1038/s43017-022-00384-8

Shcherbakova, V.V., Biggin, A.J., Veselovskiy, R.V., Shatsillo, A.V., Hawkins, L., Shcherbakov, V.P., Zhidkov, G.V., 2017. Was the devonian geomagnetic field dipolar or multipolar? Palaeointensity studies of devonian igneous rocks from the Minusa Basin (Siberia) and the Kola Peninsula Dykes, Russia. Geophys. J. Int. 209 (2), 1265–1286. https://doi.org/10.1093/gji/ggx085

Shen, F., Wen, B., McCausland, P. J.A., Gong, Z., Zhu, Z., Liu, F., Wang, J., 2025. A > 70-myr-long geomagnetic field reversal hyperactivity across the ediacaran-cambrian transition. Geophys. Res. Lett. 52 (23), e2025GL118030. https://doi.org/10.1029/2025GL118030

Soderlund, K.M., King, E.M., Aurnou, J.M., 2012. The influence of magnetic fields in planetary dynamo models. Earth Planet. Sci. Lett. 333, 9–20. https://doi.org/10.1016/j.epsl.2012.03.038

Stanley, S., 2010. A dynamo model for axisymmetrizing saturn's magnetic field. Geophys. Res. Lett. 37 (5). https://doi.org/10.1029/2009GL041752

Tassin, T., Gastine, T., Fournier, A., 2021. Geomagnetic semblance and dipolar-multipolar transition in top-heavy double-diffusive geodynamo models. Geophys. J. Int. 226 (3), 1897–1919. https://doi.org/10.1093/gji/ggab161

Terra-Nova, F., Amit, H., 2024. Regionally-triggered geomagnetic reversals. Sci. Rep. 14 (1), 9639. https://doi.org/10.1038/s41598-024-59849-z

Yan, C., Stanley, S., 2021. Recipe for a Saturn-like dynamo. AGU Adv. 2 (2), e2020AV000318. https://doi.org/10.1029/2020AV000318

Zhang, N., Zhong, S., 2011. Heat fluxes at the Earth's surface and core–mantle boundary since Pangea formation and their implications for the geomagnetic superchrons. Earth Planet. Sci. Lett. 306 (3–4), 205–216. https://doi.org/10.1016/j.epsl.2011.04.001